

Article

Single Crystal Growth and Nano-Structure Study in a Topological Dirac Metal, $\text{CoTe}_{2-\delta}$

Lei Chen ¹, Weiyao Zhao ^{2,*} and Ren-Kui Zheng ^{1,*}

¹ School of Physics and Materials Science, Guangzhou University, Guangzhou 510006, China; chenlei@gzhu.edu.cn

² Department of Materials Science & Engineering, Monash University, Clayton, VIC 3800, Australia

* Correspondence: weiyao.zhao@monash.edu (W.Z.); zrk@ustc.edu (R.-K.Z.)

Abstract: A single crystal of a topological material, $\text{CoTe}_{2-\delta}$, has been grown via the chemical vapor transport method for a structural and electronic transport study. Single-crystal X-ray diffraction, powder X-ray diffraction, and high-resolution scanning electron microscope measurements confirm the high quality of the as-grown single crystals. In a high-resolution scanning electron microscopy study, a clear layered feature of the trigonal $\text{CoTe}_{2-\delta}$ crystal was observed. Fractal features and mosaic-type nanostructures were observed on the as-grown surface and cleaved surface, respectively. The trigonal $\text{CoTe}_{2-\delta}$ demonstrates a metallic ground state in transport measurements, with a typical carrier's concentration in a 10^{21} cm^{-3} magnitude and a residual resistivity ratio of 1.6. Below 10 K, trigonal $\text{CoTe}_{2-\delta}$ contains quite complicated magnetoresistance behavior as a result of the competing effect between Dirac states and possible spin fluctuations.

Keywords: topological material; single crystal; 2D material; nanostructures



Citation: Chen, L.; Zhao, W.; Zheng, R.-K. Single Crystal Growth and Nano-Structure Study in a Topological Dirac Metal, $\text{CoTe}_{2-\delta}$. *Crystals* **2024**, *14*, 46. <https://doi.org/10.3390/cryst14010046>

Academic Editors: Artem Pronin, Dariusz Szeliga and Jacek Krawczyk

Received: 24 November 2023

Revised: 22 December 2023

Accepted: 27 December 2023

Published: 28 December 2023



Copyright: © 2023 by the authors. Licensee MDPI, Basel, Switzerland. This article is an open access article distributed under the terms and conditions of the Creative Commons Attribution (CC BY) license (<https://creativecommons.org/licenses/by/4.0/>).

1. Introduction

Transition metal dichalcogenides (TMDs) have drawn tremendous attention in both fundamental and applicational studies. In the TMD family, there are over 40 two-dimensional (2D) compounds with the general formula of MX_2 , where M is a transition metal and X is a chalcogen such as S, Se, or Te. Bulk TMDs have been widely studied over several decades for its crystal, electronic, and magnetic structures. The van der Waal bonds hold 2D layers along the *c* axis, in which the transition metal is sandwiched between two chalcogens, forming a stable structure. Therefore, like graphene exfoliated from graphite [1,2], a monolayer or few-layer TMD can be exfoliated from the bulk crystal, which could be effective wide-band semiconductors [3–9], highly efficient photoelectric units [10–16], 2D superconductors [7,17–20], building blocks in van der Waals heterostructures [21–26], and moiré superlattices [27–38].

The electronic structure of TMD bulk crystals are studied a lot in metallic or semi-metallic TMDs, such as WTe_2 , PdTe_2 , PtTe_2 , PtSe_2 , NiTe_2 , etc., in which the symmetry protected topological band structures are reported [39–41]. Topology is employed as a new type of category method on electronic band structures [42,43]. The band topology research started on the integer quantum Hall effect in two-dimensional electron gas (2DEG). Once the 2DEG is restricted in one dimension and works as an electron wave conductor, the Landau levels will change at the edges. In the center of the electron wave conductor, the LL energy is independent of the position, while near the edges, it is raised in response to the edge's potential energy. Giving a certain Fermi energy E_F , the boundary of the occupied LLs must pass through the E_F , which leaves the edge conduction channels (or edge states). This effect can only be understood using the concept of topology. In the QHE states, the bulk states are insulating, and the edge modes are free-way-like one-dimensional (1D) conduction channels, which geographically separate the carriers with opposite momentum. In conventional 1D transport, the resistance originates from the backscattering mechanism,

which mixes together the forward- and backward-moving charges. In integer quantum Hall states, however, the forward-moving charges and backward-moving charges are located at the different edges of the system, and therefore survive from the backscattering mechanism. A 2D band structure consists of mapping from the crystal momentum to the Bloch Hamiltonian. Gapped band structures can be classified topologically by considering the equivalence classes of Bloch Hamiltonian that can be continuously deformed into one another without closing the energy gap. These classes are distinguished by a topological invariant n called the Chern invariant. In quantum mechanics, a geometric phase is a phase difference acquired over a closed path, which could be nontrivial, and it was discovered by Sir Michael Berry, namely the Berry phase [44]. Another interesting quantized Hall state is the quantized version of the spin Hall effect, namely the quantum spin Hall effect (QSHE). The QSHE can be understood as the combination of spin-up QHE and spin-down QHE with its own chirality. Therefore, with the charging canceling, the total Hall conductance is zero for the QSE; however, it still presents a non-zero spin Hall conductance. At first, C. L. Kane and E. J. Mele [45] proposed a new spin orbital coupling (SOC) term in the Hamiltonian system related to Haldane's model. The SOC Hamiltonian can be taken separately for the $S_z = 1$ spins, which are equivalent to Haldane's model for spinless electrons, and also violate time reversal symmetry. This model suggests that the SOC introduces a periodic magnetic field with no net flux in the system, giving rise to a finite energy gap. At temperatures well below the gap, the double-spin Haldane's model finally leads to a quantized Hall conductance to each spin. In this situation, the edge modes are helical spin modes, which are the spin-up electron and spin-down electron with opposite momentum. Provided that the time reversal symmetry of the system (TMS) is preserved, this acts to protect the edge modes from nonmagnetic impurity and disorder. The scattered electrons have a 2π phase difference for the presence of TMS. In quantum mechanics, when the spin $1/2$ particles rotate by 2π , the wave function has a changed sign. However, in the presence of magnetic impurity, the time reversal symmetry is broken, as well as the backscattering immune transport. After the investigation in different quantum Hall states, topology was studied in solid-state materials, including, briefly, (1) a two-dimensional topological insulator, where the normal bands and inverted bands overlap in some materials (e.g., the CdTe/HgTe quantum well, in which the strong spin-orbit coupling (SOC) opens a gap at the bulk bands and leaves the bulk-symmetry protected metallic edge states); (2) a three-dimensional topological insulator (3DTI), which is the 3D form of a topological insulator, which possesses gapped bulk states and symmetry-protected metallic surface states; (3) Dirac/Weyl Semimetals, which have the bulk-symmetry protected four-fold band crossing (degeneration) points (Dirac points are found in a Dirac semimetals) and two-fold degenerate Weyl points. The Weyl points can be obtained by broken inversion symmetry, namely a Weyl semimetal, or by broken time-reversal symmetry, namely a (4) magnetic Weyl semimetal. The WTe_2 is very famous for its type-II Weyl semimetal states (with tilted Weyl cone pairs as signature) in bulk crystals [39,40], as well as 2D topological insulating states in monolayer form [46,47]. The $PdTe_2$ and $PtTe_2$ hold type-II Dirac fermions with a tilted Dirac cone near its Fermi energy due to the violation of the Lorentz symmetry [41,48]. Similarly, the TMD compound $CoTe_2$ has also attracted increasing attention recently [49–64]; it was first known as an effective electrocatalyst for hydrogen evolution reaction with low overpotentials and small Tafel slopes. The orthorhombic $CoTe_2$ is reported as a quantum critical Dirac metal with strong spin fluctuations [65]. The ferromagnetic ordering is suppressed, even at low temperatures, down to 1.8 K, and instead, a strong spin fluctuation state is proposed. The electronic band structure in orthorhombic $CoTe_2$ was predicted to harbor multiple Dirac-type nodal lines and conventional Dirac points [65]. A recent report also mentioned that the Jahn–Teller effect induces a slight distortion in the $CoTe_2$ crystal, which enriches the active site exposure in lithium–sulfur batteries [66]. The trigonal $CoTe_2$ has slightly different topology in its band structures, which is featured with a pair of type-II Dirac nodes that are located along the Γ -A direction above the Fermi energy [67,68]. In addition, multiple bulk band inversions are located in the Brillouin zone, which give rise

to a ladder of spin-polarized surface states over a wide range of energies. The surface states corresponding to the bulk band inversions form a Dirac cone at the Γ point, which has in-plane spin splitting due to Rashba-type spin–orbit interactions [67]. However, the magnetotransport properties in trigonal CoTe_2 single crystals, which will further confirm the novel electronic states, have not reported in the literature.

In this article, we reported the single crystal growth, microstructural characterization, and electronic transport properties in $\text{CoTe}_{2-\delta}$. The mosaic-like nanostructure embedded in layered crystals is exceptionally rare in TMD crystals. Negative magnetoresistance is observed at 2 K, which possibly indicates the frustrated spin dynamics.

2. Experiments

The $\text{CoTe}_{2-\delta}$ single crystals are grown using a chemical vapor transport (CVT) method, which is very popular in the single crystal growth of quantum materials [69–73], as demonstrated in Figure 1. The chemical vapor transport summarizes a variety of reactions that show one common feature: a solid-state material is volatilized in the presence of a gaseous reactant, the transport agent, and deposits elsewhere, usually in the form of single crystals. Usually, the chemical reactions happen in a closed environment, which relies on a suitable transport agent and the experimental condition. Therefore, it is a prerequisite for a transport effect in which the transport agent reacts with the source material with the formation of one or more gaseous compounds. In this case, halogens or halogen compounds are usually used as transport agents. Due to the chemical reaction that happens at the interface of solid and gas states, a relatively lower temperature condition is employed more than other crystal methods. Therefore, the CVT method shows significant advantage in high-melting-point crystal growth. In this experiment, we chose TeCl_4 as the transport agent. Briefly, high-purity Co (99.9%) and Te (99.99%) powders in a 1:2 molar ratio (~1 g in total) are sealed in a silica tube in a high vacuum, together with 5 mg/mL of TeCl_4 as transport agent. The actual transport agent's mass (TeCl_4) was calculated based on the volume of the sealed silica tube.

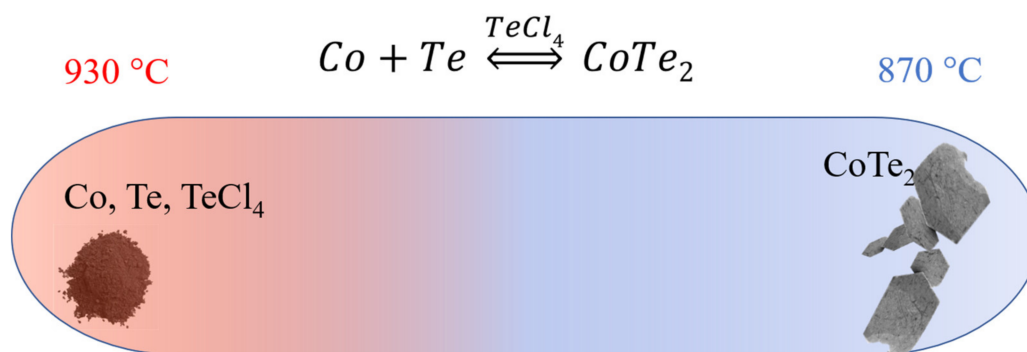


Figure 1. A sketch of the CVT crystal growth process.

It is worth mentioning that the CVT method is highly flexible in quantum material designs. For example, Z. Li et al. [74] developed a CVT-based method to prepare a large-sized Weyl semimetal tantalum arsenide crystal, which has a higher melting point than its decomposition temperature. In this case, large-size crystal growth methods like the Bridgeman method are not allowed. The sample powders and I_2 transport agent are sealed in an ampule, which is slightly tilted up to 30° from the horizon to enhance the growth rate. Particularly, one piece of polished tantalum foil was placed in the crystallization side to retard the spontaneous nucleation. In their report, a 1 cm TaAs single crystal was collected on the tantalum foil instead of small 1–3 mm crystals. Moreover, the CVT method can also be modified into a high-throughput method for doped quantum material system, e.g., topological semimetal $\text{Ta}_{1-x}\text{Nb}_x\text{Sb}_2$ [69]. In their experiments, a doping ratio of Ta:Nb at 1:1 was employed in the starting materials at a low-temperature site. After a fine-tuned growth condition is established, single crystals with various Ta:Nb ratios can be obtained.

In the crystal counting vs. chemical composition plot, a Gaussian-like distribution was observed, which supports the experimental research in quantum materials.

The sealed silica tube is placed in a dual temperature zone horizontal furnace. The Co and Te powders sit in the hot side (930 °C), which will be transported to the low-temperature site (870 °C) over one week into CoTe₂ single crystals. The obtained single crystals are of hexagonal shape and have a metallic shiny color (Figure 2a), with a ~3 mm lateral dimension and ~0.3 mm thickness. Approximately 10 pieces of high-quality single crystals can be obtained from each silica tube. The X-ray diffraction (XRD) technique (Bruker D8 Advance Eco with cobalt radiation $K_{\alpha} = 1.79 \text{ \AA}$) is employed to determine the crystal quality and orientation. The microstructure of the as-grown and cleaved crystal is characterized using scanning electron microscopy (SEM, ThermoFisher Scientific FEI Helios 5, Waltham, MA, United States). The elemental concentration mapping is conducted using an Oxford Instrument energy-dispersive spectroscopy (EDS) system equipped in Helios 5. Standard Hall-bar contacts are patterned on a freshly cleaved single crystal surface using room temperature cured silver paste for electronic transport measurements. A Physical Property Measurement System (PPMS, Quantum Design) is employed to conduct the temperature and magnetic field-dependent transport measurements in the CoTe_{2- δ} single crystal.

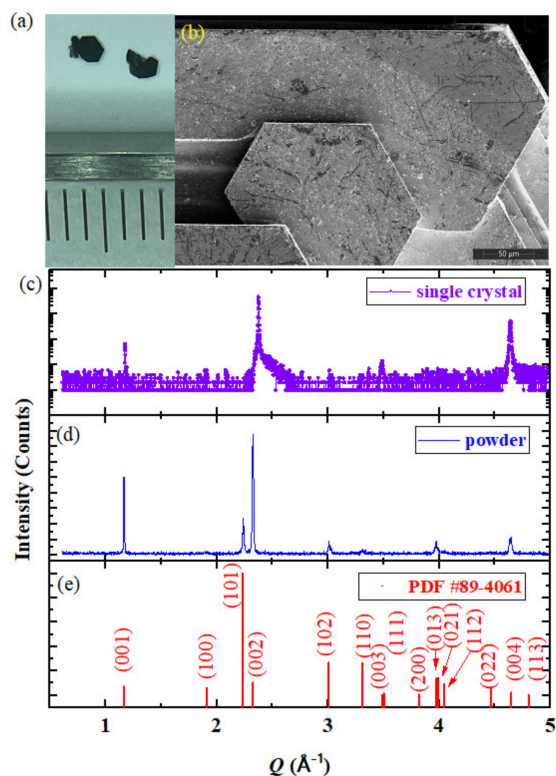


Figure 2. The structural characterizations of CoTe_{2- δ} samples. (a) Optical image of as-grown crystals. (b) The low-magnification secondary electron image. (c) The single-crystal and (d) powder XRD patterns of CoTe_{2- δ} crystals. (e) The PDF card #89-4061.

3. Results and Discussion

There are three different types of CoTe₂ that were investigated, namely trigonal CoTe₂, cubic CoTe₂, and orthorhombic CoTe₂. The single-crystal XRD pattern taken from a freshly cleaved sample surface verifies the trigonal phase, as shown in Figure 2. Thus, the obtained single crystals are hexagonal thin plates, as demonstrated in Figure 2b. Trigonal CoTe_{2- δ} crystallizes in a LiTiS₂-type structure (space group $P\bar{3}m1$), which has a typical van der Waals layered structure, and can be exfoliated along the c axis [55,57,67,68]. The cleavage faces in CoTe₂ is therefore verified as c surfaces, as indicated by the sharp (00 l) patterns in

Figure 2c. The powder XRD patterns of $\text{CoTe}_{2-\delta}$ is shown in Figure 2d. The peak intensity ratio between (101) and (002) shows a preferred orientation in the prepared powder sample, which is due to the 2D crystal structure. The standard diffraction results in the PDF card #89-4061 are plotted in Figure 2e with clear indices. Due to the different X-ray source materials used in the current experiments and PDF card, $Q = \frac{4\pi \sin\theta}{\lambda}$ was employed in Figure 2. Figure 2b shows the low-magnification SEM image via the secondary electron mode, in which one can see the overall hexagonal shape in the spontaneous crystallization procedure in the CVT set-up.

To verify the chemical composition of the as-grown single crystal, the EDS spectrum is taken on a fairly large cleaved surface area, as shown in Figure 3. The second electron image and back-scattering electron image of the same area are shown in Figure 3a,b, with an applied accelerating voltage of 18 kV. A clear layered structure can be observed in Figure 3a, in which the highlighted lines indicate the edge of the layers, and the shadowing effect can be observed next to the highlighted region. Secondary electron (SE) imaging is carried out using the surface morphology sensitive technique, and therefore shows the details of the cleaving steps. At the same area, the back-scattering electron (BSE) image shows much lower contrast, which is due to the much deeper detecting depth in back-scattering mode. Note that the BSE mode is very sensitive to crystal orientation, chemical composition, and impurity phase. The similar feature with lower contrast in the BSE images implies that the cleaved surface of CoTe_2 is from a single-crystalline phase without impurities within the resolution. In the EDS measurements, the detection is deeper than the BSE mode, and therefore it is nearly featureless in Figure 3e,f, which show the Co $K_{\alpha 1}$ and Te $K_{\alpha 1}$ mapping, respectively. The quantified analysis of the EDS spectrum on the whole surface area is shown in Figure 3c, in which the Co:Te atomic ratio of 36.1:63.9 (close to $\text{CoTe}_{1.77}$) is confirmed. In a previous study, the stabilized layered structure was reported in a Te vacancy phase ($\text{CoTe}_{1.8}$) [49], which supports the finding in our CVT-grown layered CoTe_2 . The reason for the off-stoichiometric ratio is possibly due to the deviation from a standard CdI_2 structure, in which the metal–metal bonding and interlayer covalent interactions are detected [49]. This is quite unusual for a traditional layered compound.

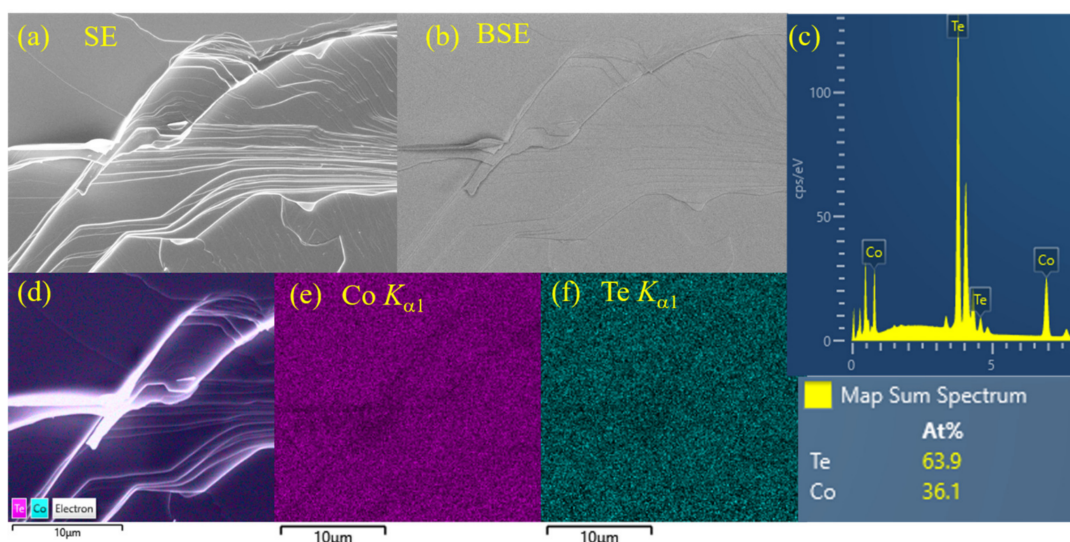


Figure 3. SEM and EDS measurements on a freshly cleaved CoTe_2 surface. (a) Secondary electron image. (b) Back-scattering image. (c) The EDS spectrum over the whole imaging area. (d) The element maps and second electron image are plotted in superposition. The element maps are shown in Panels (e) (Co) and (f) (Te) at the same position.

The surface morphologies of the $\text{CoTe}_{2-\delta}$ single crystals are further studied with the low-voltage (5 kV) SE method to demonstrate the details of the as-grown and cleaved surfaces (Figure 4). A low magnification SE image is shown in Figure 4a, in which the dark

region beyond the hexagonal crystal edges is carbon tap. The crystal is cleaved using a blue tape before imaging, which reveals a cleaved area in the bottom left region, as indicated by the arrow. To show the zoomed-in view of the surface, a double-focused method (Emersion Mode) equipped in Helios 5 is employed in Figure 4b–d,f–h. The zoomed-in views of the as-grown surface are shown in Figure 4b–d, in which Panel b demonstrates the overall flatness in a relatively large area. There are a few contamination dots on the as-grown surface with a typical dimension in several tens to hundreds of nanometers. In a further zoomed-in view of the surface area, one can observe two typical surface morphologies, as demonstrated in Figure 4c,d, which were taken from the close-to-crystal-edge area and far-from-crystal-edge area, respectively. Figure 4c demonstrates the nanoscale morphology close to the crystal edges, in which the piled-up triangles with relatively thick edge areas are observed. A higher contrast in Figure 4c is observed in this region than the contrast in the middle area of the crystals, as shown in Figure 4d. Zig-zag patterns with 60° or 120° angles are observed in the few hundred nanometers region. These fractal hexagonal features on the as-grown single-crystal surface are dominant by the crystal growth dynamics, similar to the observation in the metal-flux method. The cleaved surface shows a quite different morphology compared with the as-grown surfaces in two aspects: (1) a large, flat region without nano-size contamination is observed; (2) a clear layer feature with steps is observed in Figure 4e. With a further zoomed-in view, nano-mosaic patterns are observed everywhere on the cleaved surfaces, as demonstrated in Figure 4f–h. The mosaics, typically 20–50 nm, contain curved boundaries with different widths, showing a dry-lake-bottom-like pattern. The reason for the mosaic feature contrast in Figure 4f–h is unknown, which is also observed in flat regions (Figure 4g) and is different with the step-induced contrast in Figure 4e. As mentioned by the referee in the peer-reviewing process, a complicated chemical origination of this nanostructure is deduced. Therefore, the elemental concentration analysis method with nanometer resolution are desired to conduct further characterizations in these crystals. The surface patterns observed in Figure 4 are universal for all CVT-grown $\text{CoTe}_{2-\delta}$ single crystals using the aforementioned method. The rich surface nanostructures in trigonal $\text{CoTe}_{2-\delta}$ could contribute to the excellent electrocatalysis properties [54,56,58,59,63].

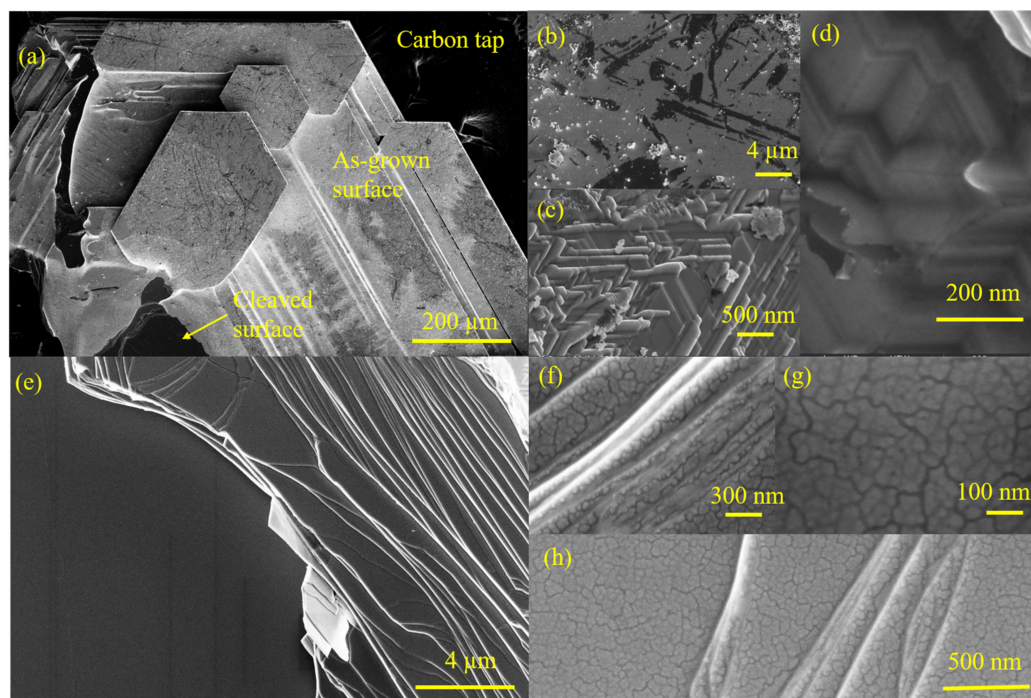


Figure 4. The low-voltage SE images of CoTe_2 single crystals. (a) Low-magnification SE image in a large area. The high magnification SE images of as-grown surface and cleaved surface are shown in Panels (b–d) and (e–h).

We then study the electronic transport properties of the CoTe₂ single crystals with nanoscale features using Hall-bar geometry patterned on a freshly cleaved crystal surface. During the measurements, the current was applied in the *c* plane, and the magnetic field was applied along the *c* axis of the crystal. Temperature (RT)- and magnetic field (MR)-dependent longitudinal resistivity are measured using the electronic transport function in PPMS, as shown in Figures 5 and 6. The resistivity is ~205 μΩ cm at room temperature, and decreases monotonically with cooling to 2 K, yielding a residual resistivity ratio of ~1.6. The longitudinal room temperature resistivity is ~180 μΩ cm in a four-terminal measurement [65] in orthorhombic CoTe₂, and ~2.5–42 mΩ cm in two-terminal measurements in trigonal CoTe₂ nanoflakes [55]. The two terminal results contain contact resistance between CoTe₂ and gold contacts, which is significantly higher than the observation here. Moreover, the similar metallic RT behavior was also reported in orthorhombic CoTe₂, with comparable resistivity in the 2–300 K region [65]. The other similar compound, NiTe₂, however, possesses a much larger RRR value (~109) and lower room temperature resistivity (~26 μΩ cm) [75]. The tellurium vacancy-induced structural change could be a reason for the different transport behaviors between NiTe₂ and CoTe_{2-δ}. We then measured the magnetic response of resistivity at low temperatures, as shown in Figure 6a. At 2 K, negative MR behavior is observed, which reaches ~−0.06% at ~4 T. The negative MR vanishes with heating, e.g., at 5 K, a positive MR up to 0.12% is observed. With further heating to 10 K, no obvious MR behavior observed. More low-field features can be observed at 2 K and 5 K, e.g., a slight upturn with magnetic fields applied from 0 to 0.5 T at 2 K, and a slightly negative MR observed at 5 K within 1 T, indicating the complicated magnetic interaction nature below 10 K in trigonal CoTe_{2-δ}.

Figure 6b shows the Hall effect at 2 K, 5 K, and 10 K, which are linear lines coinciding with each other, implying that the aforementioned low-temperature magnetic interactions have negligible contributions on the Hall effect. From the Hall curves, one may obtain the Hall coefficient, $R_H \sim 3.0 \times 10^{-9} \text{ m}^3/\text{C}$, and (hole) carrier's density, $n_h \sim 2 \times 10^{21} \text{ cm}^{-3}$. The carrier's Hall mobility at 2 K can be calculated via $\mu_{\text{Hall}} = \sigma \cdot R_H = 23 \text{ cm}^2/\text{Vs}$, where σ is the conductivity. The complicated MR behavior can be understood based on the band topology study by ARPES and spin-ARPES [67]. The ionic balance of the chemical formula suggests that the *d* electrons from Co and the *p* electrons from Te contribute to the conduction carriers on the Fermi surface. The bulk bands show multiple band inversion features throughout the Brillouin zone, which harbor Dirac cone surface states at the Γ point [67]. Linear-dispersed topological surface states will contribute to a positive linear MR at low temperatures, together with quantum interference features, e.g., weak antilocalizations. However, the overall carrier's concentration from bulk states is much higher than that of the Dirac surface states, which possibly leads to very weak MR responses. On the other hand, the absence of a hysteresis effect in MR suggests the absence of strong ferromagnetic interactions, which is similar to the observation in orthorhombic CoTe₂. In Figure 6, no anomalous Hall effect was observed, even at 2 K, which also indicates the absence of long-range magnetic ordering at this temperature. However, the short-range interactions may form at this temperature range, which indicate moderate correlations between Co moments. In this case, the crystal is probably reaching the ordering transition point, and thus is easily affected by the applied magnetic field. This magnetic field-induced ordering will reduce the magnetic disorder-induced scatterings and thus contribute to a negative MR. A significant negative MR is usually observed slightly above the magnetic ordered phase as an indication of short-range ordering, e.g., in Ti-doped Cr₂Se₃ [73], NdCrSb₃ [76]. In CoTe_{2-δ} single crystals, the negative MR behavior is probably due to the short-range magnetic interactions, in which the moments will be aligned along the magnetic field.

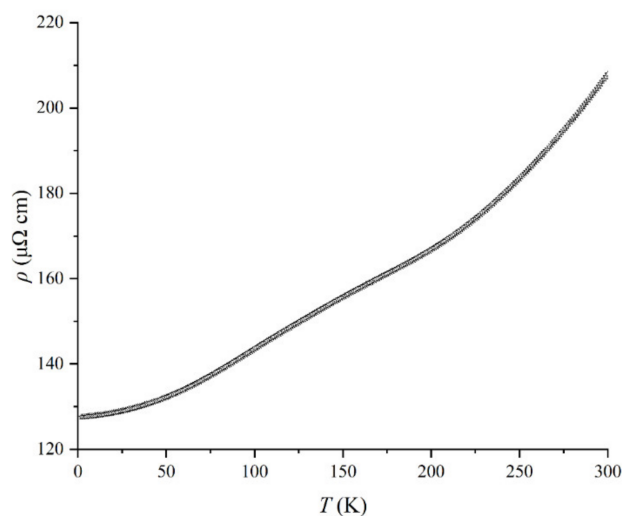


Figure 5. Temperature-dependent longitudinal resistivity behavior in 2–300 K region in a CoTe₂ single crystal.

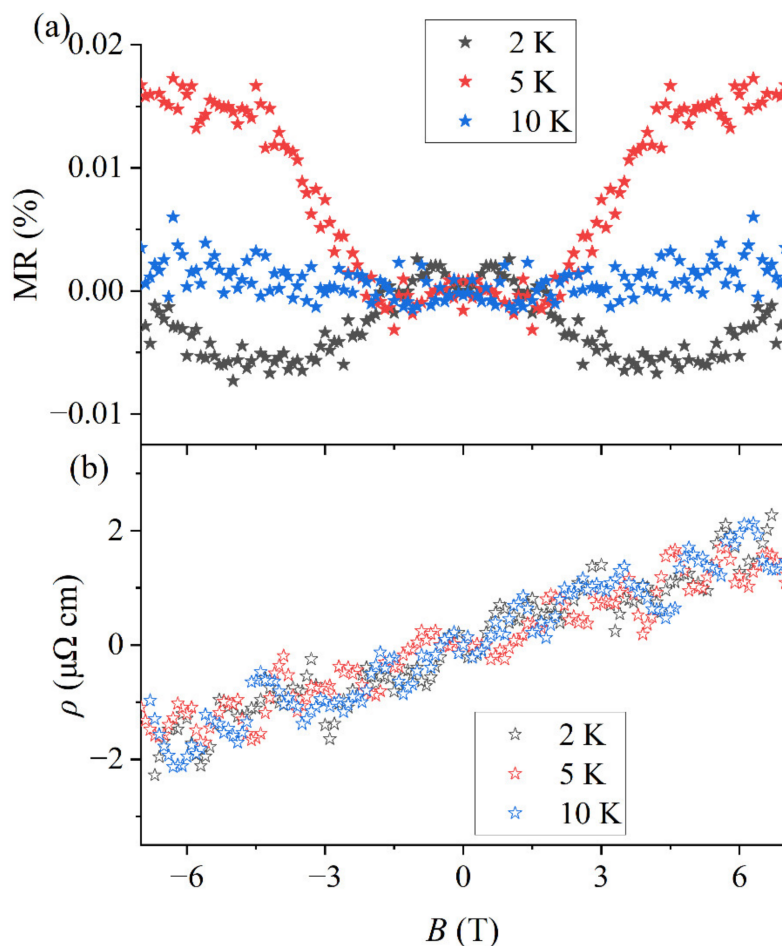


Figure 6. Magnetotransport behavior in CoTe₂ single crystal. (a) MR and (b) Hall effect are measured at 2 K, 5 K, and 10 K.

To conclude, a trigonal CoTe₂ single crystal with Te vacancies was successfully grown using the CVT method. The as-grown layered single crystals have smooth surfaces with hexagonal edges due to the crystal symmetry. Two features are observed on the as-grown single-crystal surface from the spontaneous crystal growth process: (1) piled up triangles

with relatively thicker edges appear near to the edge region, and (2) a flat region with ~100 nm zig-zag stripes can be found everywhere on the surface. On a cleaved surface, mosaic-like patterns are observed with the typical dimension of a few tens of nanometers. The CoTe₂ single crystal possesses metallic ground states, with a hole carrier concentration at a 10²¹ cm⁻³ magnitude. Below 10 K, CoTe₂ shows transport features of mixed contributions from surface Dirac fermions and short-range magnetic interactions. The bulk states are much stronger than the Dirac surface states in a sub mm thick bulk crystal, which limits the observation of strong MR and quantum interference effects. Therefore, thin flakes down to few nanometers are desired in a future study, in which the topological surface states will contribute to a higher percentage in the transport behavior. Further, mosaic patterns in TMDs are rarely reported in high-quality single crystals, which will also inspire future studies in the TMD family.

Author Contributions: Investigation and first draft writing, L.C.; Supervision, W.Z. and R.-K.Z. All authors contribute to discussion. All authors have read and agreed to the published version of the manuscript.

Funding: This research was funded by Natural Science Foundation of Guangdong Province (Grant No. 2022A1515010583), the National Natural Science Foundation of China (Grant No. 11974155), and the Bureau of Education of Guangzhou Municipality (Grant No. 202255464).

Data Availability Statement: All data are included in the article, which will be available upon reasonable request.

Conflicts of Interest: The authors declare no conflict of interest.

References

1. Novoselov, K.S.; Geim, A.K.; Morozov, S.V.; Jiang, D.; Katsnelson, M.I.; Grigorieva, I.V.; Dubonos, S.; Firsov, A.A. Two-dimensional gas of massless Dirac fermions in graphene. *Nature* **2005**, *438*, 197–200. [[CrossRef](#)]
2. Novoselov, K.S.; Geim, A.K.; Morozov, S.V.; Jiang, D.-E.; Zhang, Y.; Dubonos, S.V.; Grigorieva, I.V.; Firsov, A.A. Electric field effect in atomically thin carbon films. *Science* **2004**, *306*, 666–669. [[CrossRef](#)]
3. Bernardi, M.; Palummo, M.; Grossman, J.C. Extraordinary Sunlight Absorption and One Nanometer Thick Photovoltaics Using Two-Dimensional Monolayer Materials. *Nano Lett.* **2013**, *13*, 3664–3670. [[CrossRef](#)]
4. Kang, K.; Xie, S.E.; Huang, L.J.; Han, Y.M.; Huang, P.Y.; Mak, K.F.; Kim, C.J.; Muller, D.; Park, J. High-mobility three-atom-thick semiconducting films with wafer-scale homogeneity. *Nature* **2015**, *520*, 656–660. [[CrossRef](#)]
5. Li, H.; Wu, J.M.T.; Yin, Z.Y.; Zhang, H. Preparation and Applications of Mechanically Exfoliated Single-Layer and Multi layer MoS₂ and WSe₂ Nanosheets. *Acc. Chem. Res.* **2014**, *47*, 1067–1075. [[CrossRef](#)]
6. Liu, W.; Kang, J.H.; Sarkar, D.; Khatami, Y.; Jena, D.; Banerjee, K. Role of Metal Contacts in Designing High-Performance Monolayer n-Type WSe₂ Field Effect Transistors. *Nano Lett.* **2013**, *13*, 1983–1990. [[CrossRef](#)]
7. Lv, R.; Robinson, J.A.; Schaak, R.E.; Sun, D.; Sun, Y.F.; Mallouk, T.E.; Terrones, M. Transition Metal Dichalcogenides and Beyond: Synthesis, Properties, and Applications of Single- and Few-Layer Nanosheets. *Acc. Chem. Res.* **2015**, *48*, 56–64. [[CrossRef](#)]
8. Ugeda, M.M.; Bradley, A.J.; Shi, S.F.; da Jornada, F.H.; Zhang, Y.; Qiu, D.Y.; Ruan, W.; Mo, S.K.; Hussain, Z.; Shen, Z.X.; et al. Giant bandgap renormalization and excitonic effects in a monolayer transition metal dichalcogenide semiconductor. *Nat. Mater.* **2014**, *13*, 1091–1095. [[CrossRef](#)]
9. Wang, H.; Yu, L.L.; Lee, Y.H.; Shi, Y.M.; Hsu, A.; Chin, M.L.; Li, L.J.; Dubey, M.; Kong, J.; Palacios, T. Integrated Circuits Based on Bilayer MoS₂ Transistors. *Nano Lett.* **2012**, *12*, 4674–4680. [[CrossRef](#)]
10. Choi, W.; Ahn, J.; Kim, K.T.; Jin, H.J.; Hong, S.; Hwang, D.K.; Im, S. Ambipolar Channel p-TMD/n-Ga₂O₃ Junction Field Effect Transistors and High Speed Photo-sensing in TMD Channel. *Adv. Mater.* **2021**, *33*, 2103079. [[CrossRef](#)]
11. Kallatt, S.; Umesh, G.; Bhat, N.; Majumdar, K. Photoresponse of atomically thin MoS₂ layers and their planar heterojunctions. *Nanoscale* **2016**, *8*, 15213–15222. [[CrossRef](#)]
12. Liu, R.; Wang, F.K.; Liu, L.X.; He, X.Y.; Chen, J.Z.; Li, Y.; Zhai, T.Y. Band Alignment Engineering in Two-Dimensional Transition Metal Dichalcogenide-Based Heterostructures for Photodetectors. *Small Struct.* **2021**, *2*, 2000136. [[CrossRef](#)]
13. Liu, W.J.; Liu, M.L.; Han, H.N.; Fang, S.B.; Teng, H.; Lei, M.; Wei, Z.Y. Nonlinear optical properties of WSe₂ and MoSe₂ films and their applications in passive Q-switched erbium doped fiber lasers. *Photonics Res.* **2018**, *6*, C15–C21. [[CrossRef](#)]
14. Lu, J.P.; Liu, H.W.; Tok, E.S.; Sow, C.H. Interactions between lasers and two-dimensional transition metal dichalcogenides. *Chem. Soc. Rev.* **2016**, *45*, 2494–2515. [[CrossRef](#)]
15. Si, K.Y.; Ma, J.Y.; Lu, C.H.; Zhou, Y.X.; He, C.; Yang, D.; Wang, X.M.; Xu, X.L. A two-dimensional MoS₂/WSe₂ van der Waals heterostructure for enhanced photoelectric performance. *Appl. Surf. Sci.* **2020**, *507*, 145082. [[CrossRef](#)]

16. Zhuang, M.H.; Xu, G.L.; Gan, L.Y.; Dou, Y.B.; Sun, C.J.; Ou, X.W.; Xie, Y.Y.; Liu, Z.J.; Cai, Y.T.; Ding, Y.; et al. Sub-5 nm edge-rich 1T'-ReSe₂ as bifunctional materials for hydrogen evolution and sodium-ion storage. *Nano Energy* **2019**, *58*, 660–668. [[CrossRef](#)]
17. de la Barrera, S.C.; Sinko, M.R.; Gopalan, D.P.; Sivadas, N.; Seyler, K.L.; Watanabe, K.; Taniguchi, T.; Tsen, A.W.; Xu, X.D.; Xiao, D.; et al. Tuning Ising superconductivity with layer and spin-orbit coupling in two-dimensional transition-metal dichalcogenides. *Nat. Commun.* **2018**, *9*, 1427. [[CrossRef](#)]
18. Shi, W.; Ye, J.T.; Zhang, Y.J.; Suzuki, R.; Yoshida, M.; Miyazaki, J.; Inoue, N.; Saito, Y.; Iwasa, Y. Superconductivity Series in Transition Metal Dichalcogenides by Ionic Gating. *Sci. Rep.* **2015**, *5*, 12534. [[CrossRef](#)]
19. Sipos, B.; Kusmartseva, A.F.; Akrap, A.; Berger, H.; Forró, L.; Tutis, E. From Mott state to superconductivity in 1T-TaS₂. *Nat. Mater.* **2008**, *7*, 960–965. [[CrossRef](#)]
20. Zhou, B.T.; Yuan, N.F.Q.; Jiang, H.L.; Law, K.T. Ising superconductivity and Majorana fermions in transition-metal dichalcogenides. *Phys. Rev. B* **2016**, *93*, 180501(R). [[CrossRef](#)]
21. Baranowski, M.; Surrente, A.; Klopotoski, L.; Urban, J.M.; Zhang, N.; Maude, D.K.; Wiwatowski, K.; Mackowski, S.; Kung, Y.C.; Dumcenco, D.; et al. Probing the Interlayer Exciton Physics in a MoS₂/MoSe₂/MoS₂ van der Waals Heterostructure. *Nano Lett.* **2017**, *17*, 6360–6365. [[CrossRef](#)]
22. Calman, E.V.; Fogler, M.M.; Butov, L.V.; Hu, S.; Mishchenko, A.; Geim, A.K. Indirect excitons in van der Waals heterostructures at room temperature. *Nat. Commun.* **2018**, *9*, 1895. [[CrossRef](#)]
23. Epstein, I.; Terres, B.; Chaves, A.J.; Pusapati, V.V.; Rhodes, D.A.; Frank, B.; Zimmermann, V.; Qin, Y.; Watanabe, K.; Taniguchi, T.; et al. Near-Unity Light Absorption in a Monolayer WS₂ Van der Waals Heterostructure Cavity. *Nano Lett.* **2020**, *20*, 3545–3552. [[CrossRef](#)]
24. Ghiasi, T.S.; Ingle-Aynés, J.; Kaverzin, A.A.; van Wees, B.J. Large Proximity-Induced Spin Lifetime Anisotropy in Transition-Metal Dichalcogenide/Graphene Heterostructures. *Nano Lett.* **2017**, *17*, 7528–7532. [[CrossRef](#)]
25. Kim, J.; Jin, C.H.; Chen, B.; Cai, H.; Zhao, T.; Lee, P.; Kahn, S.; Watanabe, K.; Taniguchi, T.; Tongay, S.; et al. Observation of ultralong valley lifetime in WSe₂/MoS₂ heterostructures. *Sci. Adv.* **2017**, *3*, e1700518. [[CrossRef](#)]
26. Regan, E.C.; Wang, D.Q.; Paik, E.Y.; Zeng, Y.X.; Zhang, L.; Zhu, J.H.; MacDonald, A.H.; Deng, H.; Wang, F. Emerging exciton physics in transition metal dichalcogenide heterobilayers. *Nat. Rev. Mater.* **2022**, *7*, 778–795. [[CrossRef](#)]
27. Brotons-Gisbert, M.; Baek, H.; Molina-Sanchez, A.; Campbell, A.; Scerri, E.; White, D.; Watanabe, K.; Taniguchi, T.; Bonato, C.; Gerardot, B.D. Spin-layer locking of interlayer excitons trapped in moire potentials. *Nat. Mater.* **2020**, *19*, 630–636. [[CrossRef](#)]
28. Choi, J.H.; Hsu, W.T.; Lu, L.S.; Sun, L.Y.; Cheng, H.Y.; Lee, M.H.; Quan, J.M.; Tran, K.; Wang, C.Y.; Staab, M.; et al. Moire potential impedes interlayer exciton diffusion in van der Waals heterostructures. *Sci. Adv.* **2020**, *6*, eaba8866. [[CrossRef](#)]
29. Enaldiev, V.V.; Zólyomi, V.; Yelgel, C.; Magorrian, S.J.; Fal'ko, V.I. Stacking Domains and Dislocation Networks in Marginally Twisted Bilayers of Transition Metal Dichalcogenides. *Phys. Rev. Lett.* **2020**, *124*, 206101. [[CrossRef](#)]
30. Hennighausen, Z.; Kar, S. Twistronics: A turning point in 2D quantum materials. *Electron. Struct.* **2021**, *3*, 014004. [[CrossRef](#)]
31. Li, H.Y.; Li, S.W.; Naik, M.H.; Xie, J.X.; Li, X.Y.; Wang, J.Y.; Regan, E.; Wang, D.Q.; Zhao, W.Y.; Zhao, S.H.; et al. Imaging moire flat bands in three-dimensional reconstructed WSe₂/WS₂ superlattices. *Nat. Mater.* **2021**, *20*, 945–950. [[CrossRef](#)]
32. Maity, I.; Naik, M.H.; Maiti, P.K.; Krishnamurthy, H.R.; Jain, M. Phonons in twisted transition-metal dichalcogenide bilayers: Ultrasoft phasons and a transition from a superlubric to a pinned phase. *Phys. Rev. Res.* **2020**, *2*, 013335. [[CrossRef](#)]
33. Marcellina, E.; Liu, X.; Hu, Z.H.; Fieramosca, A.; Huang, Y.Q.; Du, W.; Liu, S.; Zhao, J.; Watanabe, K.; Taniguchi, T.; et al. Evidence for Moire Trions in Twisted MoSe₂ Homobilayers. *Nano Lett.* **2021**, *21*, 4461–4468. [[CrossRef](#)]
34. Rosenberger, M.R.; Chuang, H.J.; Phillips, M.; Oleshko, V.P.; McCreary, K.M.; Sivaram, S.V.; Hellberg, C.S.; Jonker, B.T. Twist Angle-Dependent Atomic Reconstruction and Moire Patterns in Transition Metal Dichalcogenide Heterostructures. *Acs Nano* **2020**, *14*, 4550–4558. [[CrossRef](#)]
35. Ruiz-Tijerina, D.A.; Fal'ko, V.I. Interlayer hybridization and moire superlattice minibands for electrons and excitons in heterobilayers of transition-metal dichalcogenides. *Phys. Rev. B* **2019**, *99*, 125424. [[CrossRef](#)]
36. Sung, J.; Zhou, Y.; Scuri, G.; Zólyomi, V.; Andersen, T.I.; Yoo, H.; Wild, D.S.; Joe, A.Y.; Gelly, R.J.; Heo, H.; et al. Broken mirror symmetry in excitonic response of reconstructed domains in twisted MoSe₂/MoSe₂ bilayers. *Nat. Nanotechnol.* **2020**, *15*, 750–754. [[CrossRef](#)]
37. Wilson, N.P.; Yao, W.; Shan, J.; Xu, X.D. Excitons and emergent quantum phenomena in stacked 2D semiconductors. *Nature* **2021**, *599*, 383–392. [[CrossRef](#)]
38. Xie, Y.M.; Zhang, C.P.; Hu, J.X.; Mak, K.F.; Law, K.T. Valley-Polarized Quantum Anomalous Hall State in Moire MoTe₂/WSe₂ Heterobilayers. *Phys. Rev. Lett.* **2022**, *128*, 026402. [[CrossRef](#)]
39. Ali, M.N.; Xiong, J.; Flynn, S.; Tao, J.; Gibson, Q.D.; Schoop, L.M.; Liang, T.; Haldolaarachchige, N.; Hirschberger, M.; Ong, N.P.; et al. Large, non-saturating magnetoresistance in WTe₂. *Nature* **2014**, *514*, 205–208. [[CrossRef](#)]
40. Soluyanov, A.A.; Gresch, D.; Wang, Z.J.; Wu, Q.S.; Troyer, M.; Dai, X.; Bernevig, B.A. Type-II Weyl semimetals. *Nature* **2015**, *527*, 495–498. [[CrossRef](#)]
41. Yan, M.Z.; Huang, H.Q.; Zhang, K.N.; Wang, E.Y.; Yao, W.; Deng, K.; Wan, G.L.; Zhang, H.Y.; Arita, M.; Yang, H.T.; et al. Lorentz-violating type-II Dirac fermions in transition metal dichalcogenide PtTe₂. *Nat. Commun.* **2017**, *8*, 257. [[CrossRef](#)] [[PubMed](#)]
42. Hasan, M.Z.; Kane, C.L. Colloquium: Topological insulators. *Rev. Mod. Phys.* **2010**, *82*, 3045–3067. [[CrossRef](#)]
43. Qi, X.L.; Zhang, S.C. Topological insulators and superconductors. *Rev. Mod. Phys.* **2011**, *83*, 1057. [[CrossRef](#)]

44. Zhao, W.; Wang, X. Berry phase in quantum oscillations of topological materials. *Adv. Phys. X* **2022**, *7*, 2064230. [[CrossRef](#)]
45. Fu, L.; Kane, C.L. Topological insulators with inversion symmetry. *Phys. Rev. B* **2007**, *76*, 045302. [[CrossRef](#)]
46. Fei, Z.Y.; Palomaki, T.; Wu, S.F.; Zhao, W.J.; Cai, X.H.; Sun, B.S.; Nguyen, P.; Finney, J.; Xu, X.D.; Cobden, D.H. Edge conduction in monolayer WTe₂. *Nat. Phys.* **2017**, *13*, 677–682. [[CrossRef](#)]
47. Tang, S.J.; Zhang, C.F.; Wong, D.; Pedramrazi, Z.; Tsai, H.Z.; Jia, C.J.; Moritz, B.; Claassen, M.; Ryu, H.; Kahn, S.; et al. Quantum spin Hall state in monolayer 1T'-WTe₂. *Nat. Phys.* **2017**, *13*, 683–687. [[CrossRef](#)]
48. Chia, X.Y.; Adriano, A.; Lazar, P.; Sofer, Z.; Luxa, J.; Pumera, M. Layered Platinum Dichalcogenides (PtS₂, PtSe₂, and PtTe₂) Electrocatalysis: Monotonic Dependence on the Chalcogen Size. *Adv. Funct. Mater.* **2016**, *26*, 4306–4318. [[CrossRef](#)]
49. Chia, X.Y.; Sofer, Z.; Luxa, J.; Pumera, M. Unconventionally Layered CoTe₂ and NiTe₂ as Electrocatalysts for Hydrogen Evolution. *Chem. A Eur. J.* **2017**, *23*, 11719–11726. [[CrossRef](#)]
50. Ganesan, V.; Nam, K.H.; Park, C.M. Robust Polyhedral CoTe₂-C Nanocomposites as High-Performance Li- and Na-Ion Battery Anodes. *ACS Appl. Energy Mater.* **2020**, *3*, 4877–4887. [[CrossRef](#)]
51. Gao, Q.; Huang, C.Q.; Ju, Y.M.; Gao, M.R.; Liu, J.W.; An, D.; Cui, C.H.; Zheng, Y.R.; Li, W.X.; Yu, S.H. Phase-Selective Syntheses of Cobalt Telluride Nanofleeces for Efficient Oxygen Evolution Catalysts. *Angew. Chem. -Int. Ed.* **2017**, *56*, 7769–7773. [[CrossRef](#)] [[PubMed](#)]
52. Ji, L.; Wang, Z.C.; Wang, H.; Shi, X.F.; Asiri, A.M.; Sun, X.P. Hierarchical CoTe₂ Nanowire Array: An Effective Oxygen Evolution Catalyst in Alkaline Media. *Acs Sustain. Chem. Eng.* **2018**, *6*, 4481–4485. [[CrossRef](#)]
53. Liu, M.; Lu, X.Q.; Guo, C.; Wang, Z.J.; Li, Y.P.; Lin, Y.; Zhou, Y.; Wang, S.T.; Zhang, J. Architecting a Mesoporous N-Doped Graphitic Carbon Framework Encapsulating CoTe₂ as an Efficient Oxygen Evolution Electrocatalyst. *ACS Appl. Mater. Interfaces* **2017**, *9*, 36146–36153. [[CrossRef](#)] [[PubMed](#)]
54. Lu, T.H.; Chen, C.J.; Basu, M.; Ma, C.G.; Liu, R.S. The CoTe₂ nanostructure: An efficient and robust catalyst for hydrogen evolution. *Chem. Commun.* **2015**, *51*, 17012–17015. [[CrossRef](#)] [[PubMed](#)]
55. Ma, H.F.; Dang, W.Q.; Yang, X.D.; Li, B.; Zhang, Z.W.; Chen, P.; Liu, Y.; Wan, Z.; Qian, Q.; Luo, J.; et al. Chemical Vapor Deposition Growth of Single Crystalline CoTe₂ Nanosheets with Tunable Thickness and Electronic Properties. *Chem. Mater.* **2018**, *30*, 8891–8896. [[CrossRef](#)]
56. McKendry, I.G.; Thenuwara, A.C.; Sun, J.W.; Peng, H.W.; Perdew, J.P.; Strongin, D.R.; Zdilla, M.J. Water Oxidation Catalyzed by Cobalt Oxide Supported on the Mattagamite Phase of CoTe₂. *ACS Catal.* **2016**, *6*, 7393–7397. [[CrossRef](#)]
57. Muhler, M.; Bensch, W.; Schur, M. Preparation, crystal structures, experimental and theoretical electronic band structures of cobalt tellurides in the composition range CoTe_{1.3}-CoTe₂. *J. Phys. -Condens. Matter* **1998**, *10*, 2947–2962. [[CrossRef](#)]
58. Nath, M.; De Silva, U.; Singh, H.; Perkins, M.; Liyanage, W.P.R.; Umapathi, S.; Chakravarty, S.; Masud, J. Cobalt Telluride: A Highly Efficient Trifunctional Electrocatalyst for Water Splitting and Oxygen Reduction. *ACS Appl. Energy Mater.* **2021**, *4*, 8158–8174. [[CrossRef](#)]
59. Wang, K.; Ye, Z.G.; Liu, C.Q.; Xi, D.; Zhou, C.J.; Shi, Z.Q.; Xia, H.Y.; Liu, G.W.; Qiao, G.J. Morphology-Controllable Synthesis of Cobalt Telluride Branched Nanostructures on Carbon Fiber Paper as Electrocatalysts for Hydrogen Evolution Reaction. *ACS Appl. Mater. Interfaces* **2016**, *8*, 2910–2916. [[CrossRef](#)]
60. Wang, X.; Huang, X.K.; Gao, W.B.; Tang, Y.; Jiang, P.B.; Lan, K.; Yang, R.Z.; Wang, B.; Li, R. Metal-organic framework derived CoTe₂ encapsulated in nitrogen-doped carbon nanotube frameworks: A high-efficiency bifunctional electrocatalyst for overall water splitting. *J. Mater. Chem. A* **2018**, *6*, 3684–3691. [[CrossRef](#)]
61. Wang, X.G.; Zhou, Z.; Zhang, P.; Zhang, S.Q.; Ma, Y.; Yang, W.W.; Wang, H.; Li, B.X.; Meng, L.J.; Jiang, H.N.; et al. Thickness-Controlled Synthesis of CoX₂ (X = S, Se, and Te) Single Crystalline 2D Layers with Linear Magnetoresistance and High Conductivity. *Chem. Mater.* **2020**, *32*, 2321–2329. [[CrossRef](#)]
62. Wang, Z.Q.; Ren, X.; Wang, L.; Cui, G.W.; Wang, H.J.; Sun, X.P. A hierarchical CoTe₂-MnTe₂ hybrid nanowire array enables high activity for oxygen evolution reactions. *Chem. Commun.* **2018**, *54*, 10993–10996. [[CrossRef](#)] [[PubMed](#)]
63. Yin, Y.Q.; Xu, J.; Guo, W.; Wang, Z.; Du, X.D.; Chen, C.; Zheng, Z.J.; Liu, D.; Qu, D.Y.; Xie, Z.Z.; et al. A single-step fabrication of CoTe₂ nanofilm electrode toward efficient overall water splitting. *Electrochim. Acta* **2019**, *307*, 451–458. [[CrossRef](#)]
64. Zhang, B.; Zhang, Y.; Li, J.L.; Liu, J.; Huo, X.G.; Kang, F.Y. In situ growth of metal-organic framework-derived CoTe₂ nanoparticles@nitrogen-doped porous carbon polyhedral composites as novel cathodes for rechargeable aluminum-ion batteries. *J. Mater. Chem. A* **2020**, *8*, 5535–5545. [[CrossRef](#)]
65. Siegfried, P.E.; Bhandari, H.; Qi, J.N.; Ghimire, R.; Joshi, J.; Messegee, Z.T.; Beeson, W.B.; Liu, K.; Ghimire, M.P.; Dang, Y.L.; et al. CoTe₂: A Quantum Critical Dirac Metal with Strong Spin Fluctuations. *Adv. Mater.* **2023**, *35*, 2300640. [[CrossRef](#)] [[PubMed](#)]
66. Wang, B.; Wang, L.; Ding, D.; Zhai, Y.; Wang, F.; Jing, Z.; Yang, X.; Kong, Y.; Qian, Y.; Xu, L. Zinc-Assisted Cobalt Ditelluride Polyhedra Inducing Lattice Strain to Endow Efficient Adsorption-Catalysis for High-Energy Lithium-Sulfur Batteries. *Adv. Mater.* **2022**, *34*, 2204403. [[CrossRef](#)] [[PubMed](#)]
67. Chakraborty, A.; Fujii, J.; Kuo, C.N.; Lue, C.S.; Politano, A.; Vobornik, I.; Agarwal, A. Observation of highly anisotropic bulk dispersion and spin-polarized topological surface states in CoTe₂. *Phys. Rev. B* **2023**, *107*, 085406. [[CrossRef](#)]
68. Hu, Z.; Zhang, L.B.; Chakraborty, A.; D'Olimpio, G.; Fujii, J.; Ge, A.P.; Zhou, Y.C.; Liu, C.L.; Agarwal, A.; Vobornik, I.; et al. Terahertz Nonlinear Hall Rectifiers Based on Spin-Polarized Topological Electronic States in 1T-CoTe₂. *Adv. Mater.* **2023**, *35*, 2209557. [[CrossRef](#)]

69. Guo, L.; Xu, M.; Chen, L.; Huang, X.; Shi, X.Y.; Ying, J.S.; Zhang, T.; Zhao, W.Y.; Dong, S.; Zheng, R.K. Electronic Transport Properties of Nb_{1-x}Ta_xSb₂ Single-Crystal Semimetals Grown by a Chemical Vapor Transport Based High-Throughput Method. *Cryst. Growth Des.* **2021**, *21*, 653–662. [[CrossRef](#)]
70. Guo, L.; Zhao, W.Y.; Ding, N.; Shi, X.Y.; Xu, M.; Chen, L.; Gao, G.Y.; Dong, S.; Zheng, R.K. Magnetotransport properties of square-net compounds of NbSiSb and NbGeSb single crystals. *J. Phys. Condens. Matter* **2020**, *32*, 435701. [[CrossRef](#)]
71. Wu, J.; Zhang, C.L.; Yan, J.M.; Chen, L.; Guo, L.; Chen, T.W.; Gao, G.Y.; Fei, L.F.; Zhao, W.Y.; Chai, Y.; et al. Magnetotransport and magnetic properties of the layered noncollinear antiferromagnetic Cr₂Se₃ single crystals. *J. Phys. Condens. Matter* **2020**, *32*, 475801. [[CrossRef](#)] [[PubMed](#)]
72. Xu, M.; Guo, L.; Chen, L.; Zhang, Y.; Li, S.S.; Zhao, W.Y.; Wang, X.L.; Dong, S.; Zheng, R.K. Emerging weak antilocalization effect in Ta_{0.7}Nb_{0.3}Sb₂ semimetal single crystals. *Front. Phys.* **2023**, *18*, 13304. [[CrossRef](#)]
73. Zhang, S.J.; Yan, J.M.; Tang, F.; Wu, J.; Dong, W.Q.; Zhang, D.W.; Luo, F.S.; Chen, L.; Fang, Y.; Zhang, T.; et al. Colossal Magnetoresistance in Ti Lightly Doped Cr₂Se₃ Single Crystals with a Layered Structure. *ACS Appl. Mater. Interfaces* **2021**, *13*, 58949–58955. [[CrossRef](#)] [[PubMed](#)]
74. Li, Z.; Chen, H.; Jin, S.; Gan, D.; Wang, W.; Guo, L.; Chen, X. Weyl semimetal TaAs: Crystal growth, morphology, and thermodynamics. *Cryst. Growth Des.* **2016**, *16*, 1172–1175. [[CrossRef](#)]
75. Liu, Q.; Fei, F.; Chen, B.; Bo, X.; Wei, B.; Zhang, S.; Zhang, M.; Xie, F.; Naveed, M.; Wan, X. Nontopological origin of the planar Hall effect in the type-II Dirac semimetal NiTe₂. *Phys. Rev. B* **2019**, *99*, 155119. [[CrossRef](#)]
76. Chen, L.; Zhao, W.; Wang, Z.; Tang, F.; Fang, Y.; Zeng, Z.; Xia, Z.; Cheng, Z.; Cortie, D.L.; Rule, K.C. Spin Reorientation Transition and Negative Magnetoresistance in Ferromagnetic NdCrSb₃ Single Crystals. *Materials* **2023**, *16*, 1736. [[CrossRef](#)]

Disclaimer/Publisher's Note: The statements, opinions and data contained in all publications are solely those of the individual author(s) and contributor(s) and not of MDPI and/or the editor(s). MDPI and/or the editor(s) disclaim responsibility for any injury to people or property resulting from any ideas, methods, instructions or products referred to in the content.